

# **Ballistic-diffusive Phonon Transport in Cellulose Nanocrystals by ReaxFF Molecular Dynamics Simulations**

Ruo-Yu Dong<sup>1, 2</sup>, Yuan Dong<sup>\*1, 3</sup>, Qianwei Li<sup>4</sup>, Caixia Wan<sup>4</sup>

<sup>1</sup> School of Mechanical Engineering, Hangzhou Dianzi University, Hangzhou, 310018, China.

<sup>2</sup> Center for Soft and Living Matter, Institute for Basic Science (IBS), Ulsan 44919, South Korea.

<sup>3</sup> Department of Mechanical and Aerospace Engineering, University of Missouri, Columbia, MO, 65201, United States.

<sup>4</sup> Department of Biomedical, Biological, and Chemical Engineering, University of Missouri, Columbia, MO, 65201, United States.

**Corresponding Author: (Y.D.) [dony327@163.com](mailto:dony327@163.com), [dongyu@missouri.edu](mailto:dongyu@missouri.edu)**

## **Abstract**

Cellulose nanocrystals (CNCs), a ubiquitous nano-sized natural biopolymer, have drawn considerable attention in recent years due to their excellent mechanical and chemical properties. However, thermal properties of CNCs, which are critical for their potential applications as structural or functional materials, are less investigated. In this work, their thermal properties were systematically studied by molecular dynamics (MD) simulations in terms of the effects of polymorphs, size, temperature, and strain. It was found that the thermal conductivities depend on the polymorphs of CNCs, but the thermal conductance of unit chain of each polymorph is similar. Moreover, the strong dependence of the thermal conductivities of CNCs on their length and

cross-sectional area indicates the existence of remarkable ballistic-diffusive phonon transport. Single chain CNCs can achieve a thermal conductivity of  $\sim 6 \text{ W/(m}\cdot\text{K)}$ , implying their potential as high thermal conductive polymer. The mechanical strain can enhance the alignment of cellulose skeleton, which reduces phonon scattering and thus increases thermal conductivity. Possible underlying mechanism of the varying thermal conductivity was further discussed and attributed to the shift of phonon frequencies and varied degree of orientation. This study reveals the sophisticated ballistic-diffusive phonon transport in CNCs, and pave path to future design of CNC-based materials with desirable thermal properties.

**Keywords:** cellulose nanocrystal; thermal conductivity; phonon transport; mechanical strain; molecular dynamics.

## Nomenclature

$A$	Cross-sectional area [ $\text{nm}^2$ ]
$a, b, c$	Crystal unit cell length [ $\text{\AA}$ ]
$D$	Phonon density of states
$e$	Unit vector
$L$	Chain length [ $\text{nm}$ ]
$l$	Phonon mean free path [ $\text{nm}$ ]
$M$	Mass [ $\text{g}$ ]
$P_2$	Orientalional order parameter
$Q$	Heat flux [ $\text{eV/ps}$ ]
$q$	Heat flux density [ $\text{W/m}^2$ ]

$R_g$	Radius of gyration [ $\text{\AA}$ ]
$T$	Temperature [K]
$TC$	Thermal conductance [pW/K]

### Greek symbols

$\alpha, \beta, \gamma$	Crystal unit cell angles [ $^\circ$ ]
$\lambda$	Thermal conductivity [W/(m·K)]
$v$	Atomic velocity [m/s]
$\omega$	Frequency (Hz)

### Subscripts

cm	Center of mass
$i$	Particle number
$\infty$	Infinite

### Abbreviations

CNC	Cellulose nanocrystal
MD	Molecular dynamics
MFP	Mean free path

## 1. Introduction

Cellulose is the most abundant biopolymer on earth and has been widely used as engineering materials to produce paper, textiles, *etc.* for thousands of years [1]. Over the past several decades, cellulose at nanoscale, also called nanocellulose, has attracted significant attention. In particular, cellulose nanocrystals (CNCs), which serves as the backbone of

nanocellulose and can be extracted by removing amorphous region from cellulose chain [1,2], are emerging renewable nanomaterials due to intrinsic properties, such as high strength and stiffness, light weight, and biodegradability [3]. With appropriate treatment, the properties of CNCs shown at nanoscale can also be readily transferred to macroscale, broadening their potential applications. For example, using flow-assisted assembly, the fabricated macroscale fibers with highly aligned nanofibrils show exceptional mechanical properties exceeding other natural and commercial bio-based materials, such as dragline silk [4]. The “super wood”, obtained by a two-step process enabling the complete densification of natural wood, achieves strength and toughness comparable to steel, but is much lighter, simpler to process, and more environmentally friendly [5]. Recently reported “cooling wood” [6], which manifests backscatter behavior to solar radiation and strong emission in mid-infrared wavelengths, also points to the fascinating opportunities of CNCs used as structural materials with exceptional thermal performance. Moreover, CNCs are also explored for other applications, such as biodegradable electronics [7], batteries [8], and optical films [9]. Thermal design is critical in all the above applications, which requires a deeper understanding of thermal properties of CNCs.

Cellulose fibers are traditionally used as thermal insulation materials in the form of loosely filled paper [10], low-density foams [11] and aerogels [12]. These materials typically exhibit a thermal conductivity close to or lower than air ( $\sim 0.03 \text{ W}/(\text{m}\cdot\text{K})$ ) [13], which can be attributed to their sponge-like structures [14]. Besides cellulose, other model bulk polymers, such as epoxy, Nylon, polyvinyl chloride, rubber, also have very low thermal conductivities in the order of  $0.1\sim 0.5 \text{ W}/(\text{m}\cdot\text{K})$  [15]. An individual crystalline polyethylene (PE) chain, however, could achieve very high ( $\sim 350 \text{ W}/(\text{m}\cdot\text{K})$ ) and possibly divergent thermal conductivity as predicted by molecular dynamics (MD) simulations [15]. Such drastic increase in thermal

conductivity can be attributed to the low-dimensional nature of a single chain, where ballistic-diffusive phonon transport dominates. Further increase in thermal conductivity is also possible by increasing crystallite orientation and crystallinity at nanoscale [16,17]. Shen et al. reported that the thermal conductivity of ultra-drawn PE nanofibers reaches as high as  $\sim 104 \text{ W}/(\text{m}\cdot\text{K})$  [18]. The stretching process aligns the atoms in crystalline domain, improves the fiber quality toward an 'ideal' single crystalline fiber, and greatly decreases phonon scattering. Similar to crystalline domain, recent studies also pointed out that increasing chain alignment in amorphous domain can also lead to a remarkable increase in thermal conductivity [19,20]. All these studies have demonstrated that thermal conductivity of polymers can be much enhanced through deliberate treatments, which can be realized by extracting polymer fibers at nanoscale in the form of low-dimensional material and further properly stretching and aligning the polymer chains. This phenomenon inspires much interest considering many key attributes of polymer, such as low cost, anti-corrosion, light weight, and insulation [21]. Herein, we hypothesize that the similar rules can also be applied to the thermal conductivity of CNCs, which is the structural unit of biopolymer cellulose.

There is little research concerning the heat conduction mechanism at nanoscale for CNCs. The experimental study reported by Uetani et al. [14] revealed the increase of in-plane heat diffusivity of cellulose nanopaper with crystallinity as a result of the phonon scattering effect with the grain boundary. They also aligned cellulose nanofibers by stretching bacterial cellulose hydrogel and found the positive correlation between the thermal conductivity along the drawing direction and the orientational order parameter [22]. Diaz et al. [23] studied the interfacial thermal resistance between nanocellulose fibers by MD simulations and found a relatively small value of 9.4 to 12.6  $\text{m}^2\text{K}/\text{GW}$ , which is even lower than that of typical thermoelectric alloys or

carbon nanotubes. Other studies mainly utilized CNCs as polymer matrix and combined them with various nanofillers to achieve high heat dissipation efficiency [24]. However, there is a lack of deeper understanding of the thermal conductivity of CNCs with phonon properties considered. To enable the use of CNCs as thermal conductive nanomaterials, it is essential to conduct systematic investigation to deeply understand their heat conduct mechanisms.

In the current work, nonequilibrium MD (NEMD) simulations was used to probe the thermal conductivity of CNCs. MD simulations have been extensively used to investigate the effects of various parameters [25] (e.g., temperature [26], bonding/non-bonding contributions [27], chain length and stiffness [28], crystallinity [29], topology [30], and stretching [31]) on the thermal properties of model polymer systems, such as PE [26,29], poly(methyl methacrylate) (PMMA) [27], and polydimethylsiloxane (PDMS) [28]. The dependence of thermal conductivity on system size and temperature was studied by varying the crystalline type of CNCs. The correlation between orientational order of CNCs based on tensile strain and thermal conductivity was also studied. The simulation results were further corroborated by polymer morphology analyses and calculated phonon density of states. Compared to the previous work by Diaz et al. [23], we provided a comprehensive and systematic study of various effects on the thermal conductivity of CNCs at the nanoscale, with the special focus on the ballistic-diffusive behavior of phonon transport. This study would further the understanding of thermal transport in nanocrystalline polymer systems, and provide useful information for the rational development of design strategies for enhanced thermal properties.

## **2. Methods**

Cellulose is a linear chain of 1-4 linked  $\beta$ -D glucopyranose with the repeating unit shown in Fig. 1a [1]. There are several known polymorphs of crystalline cellulose, including  $I\alpha$ ,  $I\beta$ , II,

III<sub>1</sub>, III<sub>2</sub>, IV<sub>1</sub> and IV<sub>2</sub>, which can be interconverted [32]. Cellulose I, sometimes referred as the native cellulose, is the form found in plants (*I* $\beta$ ), algae and bacteria (*I* $\alpha$ ) [1]. In this work, four polymorphs, namely *I* $\alpha$ , *I* $\beta$ , II, III<sub>1</sub> were chosen to calculate their thermal conductivities while focusing more on *I* $\beta$  as it is the most extensively studied form. The crystalline structures of these CNCs were generated from Cellulose-builder [33], and their unit-cell parameters are summarized in Table 1. Fig. 1b shows the 2D projection views for all the four CNC polymorphs on the *ab* plane (perpendicular to the chain direction) and *ac* plane. Cellulose *I* $\beta$ , II, III<sub>1</sub> crystal structures belong to the monoclinic P2<sub>1</sub> spatial group, whereas *I* $\alpha$  crystal structure belongs to the triclinic P1 spatial group [33].

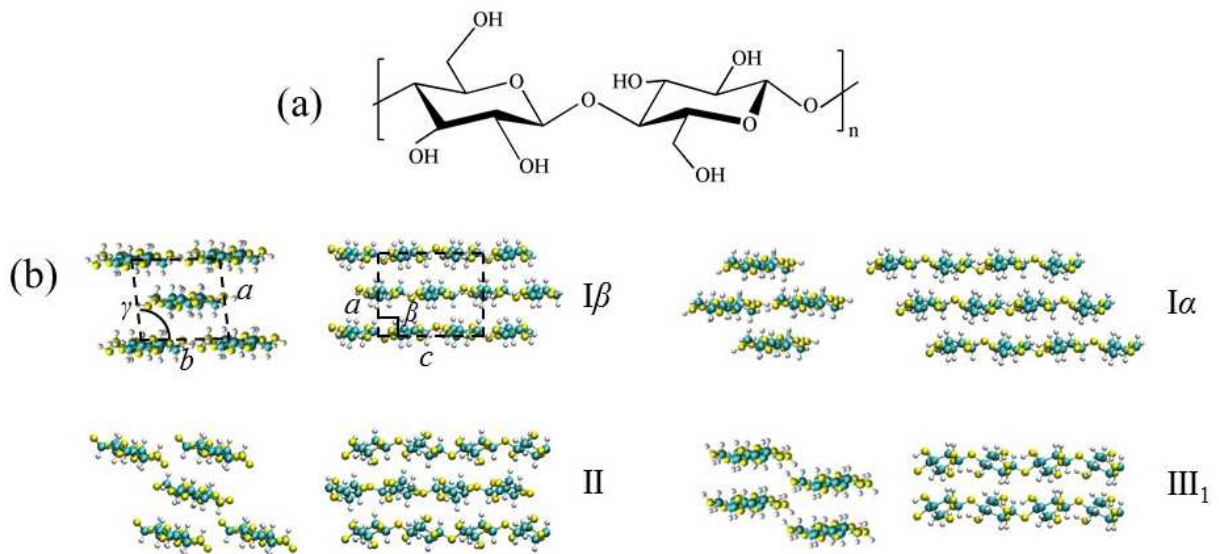


Figure 1. (a) Repeating unit of CNCs. (b) 2D projection views on the *ab* plane and *ac* plane for CNC polymorphs *I* $\beta$ , *I* $\alpha$ , II, III<sub>1</sub>. The C, H, O atoms are shown in cyan, white, and yellow, respectively.

The MD simulations were performed using the LAMMPS package [34]. Reactive force field (ReaxFF) [35,36], which has been used to study the thermal conductivity of 1D octanediol derivatives [37] and 2D polymeric graphitic carbon nitrides [38], was employed in this work. ReaxFF force field parameter values were obtained by optimization against a training set that contained data from quantum mechanical calculations. The intramolecular potential energies are expressed as a function of bond orders, including both bonded and non-bonded contributions. The ReaxFF potential was already incorporated in the LAMMPS package and we adopted the force field parameters from Ref. [36] to describe the interaction between C-H-O in cellulose by using the “pair\_coeff” command. Comparing to other non-reactive force fields, ReaxFF is expected to offer more realistic depiction of anharmonicity [39], which would be a critical factor to accurately reproduce the thermal properties of polymer systems.

Table 1. List of unit-cell parameters for CNC polymorphs  $I\alpha$ ,  $I\beta$ , II, and  $III_1$  [33].

	$a$ (Å)	$b$ (Å)	$c$ (Å)	$\alpha$ ( $^\circ$ )	$\beta$ ( $^\circ$ )	$\gamma$ ( $^\circ$ )
$I\alpha$	6.717	5.962	10.4	118.08	114.08	80.37
$I\beta$	7.784	8.201	10.38	90.0	90.0	96.5
II	8.10	9.03	10.31	90.0	90.0	117.1
$III_1$	4.45	7.85	10.31	90.0	90.0	r105.1

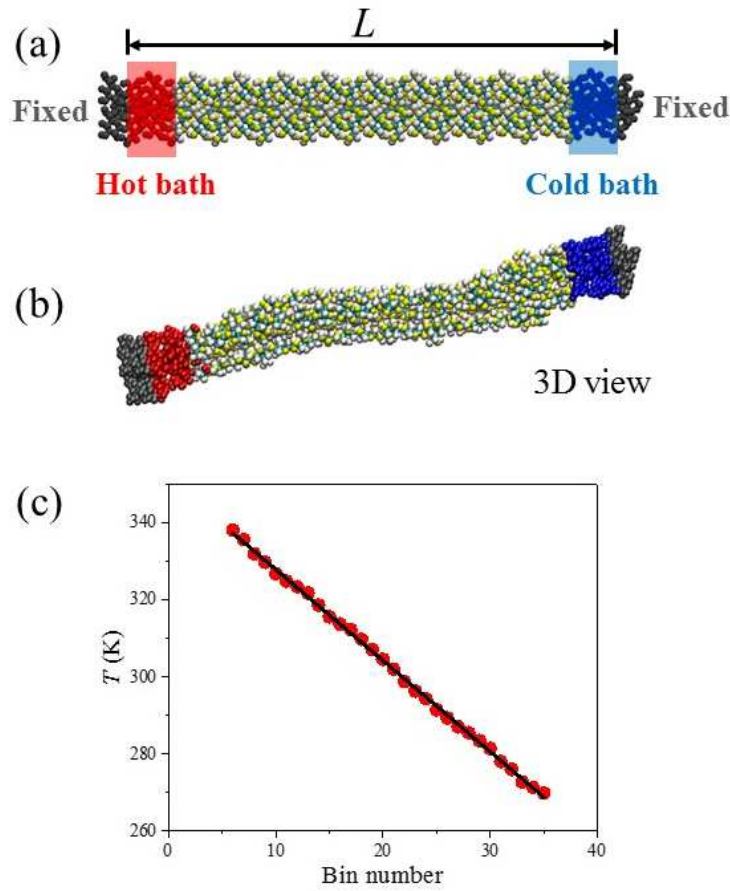


Figure 2. (a) Scheme of the simulation system, where the gray region is the fixed part. Heat flux is applied to the CNCs through a hot (red region) and a cold (blue region) bath. (b) The 3D view of the disordered CNC after 0.1 ns  $NVT$  equilibration. (c) A representative temperature profile and the linear fitting of  $I\beta$  CNC with effective chain length  $L=11.4$  nm and cross-sectional area  $A=1.58$  nm<sup>2</sup>.

The time step was set to 0.1 fs for all the simulations with periodic boundary conditions applied along all the Cartesian directions. At least 10 nm distance between two periodic images in every direction was left to avoid image-image interference. Systems were first equilibrated under an  $NVT$  ensemble for 0.5 ns, and relaxed under an  $NVE$  ensemble for another 0.5 ns. Then

we imposed thermal gradient along the  $c$  axis of CNCs by adding a hot bath and a cold bath adjacent to the two fixed ends of the system, as shown in Fig. 2a. Similar to our previous work [38], a fixed amount of energy was added to the hot region by scaling the velocity of each atom at each time step in order to conserve the total momentum, while the same amount of energy was subtracted from the cold region in the same manner. The energy exchanging rate  $q$  over the cross-sectional areas ( $A$ ) of the systems was calculated as  $q = Q/A$ , where  $Q$  varies from 0.1 to 0.4 eV/ps. After the first 0.2 ns for the system to achieve steady state, we started to collect the temperature data for another 0.3 ns. The systems, with the exception of the fixed regions, were divided into 30 segments along the length direction, which is the effective part for temperature collection.

The thermal conductivity  $\lambda$  was calculated according to the Fourier's law,

$$\lambda = -q / (dT/dx) \quad (1)$$

where  $dT/dx$  is the temperature gradient. Here at the nanoscale, the thermal conductivity  $\lambda$  extracted by using the Fourier's law should be regarded as an "effective" thermal conductivity  $\lambda_{\text{eff}}$ , as ballistic thermal transport becomes important. This definition on one hand is to distinguish the  $\lambda$  value that we are obtaining here from the bulk value, which is the intrinsic property of the materials. On the other hand, it provides direct comparison between these two and helps to reveal the nanoscale-induced behavior, e.g. the length dependence. The cross-sectional area was calculated based on the unit-cell parameters in Table 1 and the number of unit cells. For instance, the cross section of  $I\beta$  in Fig. 1b has an area of  $A = 2.5 \cdot a \cdot b \cdot \sin \gamma = 1.58 \text{ nm}^2$ , as the five chains occupy 2.5 unit cells. As shown in Fig. 2b, the initial CNC chains with perfect lattice become disordered after some simulation time. A typical temperature profile of  $I\beta$  CNC

with effective chain length  $L=11.4$  nm and cross-sectional area  $A=1.58$  nm<sup>2</sup> at system temperature 300 K is shown in Fig. 2c. Five independent runs were performed and the results were averaged to obtain each  $\lambda$  data point.

To study the dependence of thermal conductivity of CNCs on chain alignment, we applied mechanical strains uniaxially along the  $c$  axis, the same direction as the temperature gradient is applied. A constant strain rate of  $10^8$  s<sup>-1</sup> was used [38], and the simulations were performed in an  $NPT$  ensemble with constant pressure at 1 atm. During the drawing process, we extracted the intermediate configurations at different tensile strains and used them as the initial conditions for thermal conductivity simulations. The above procedures, including system equilibration with  $NVT$ ,  $NVE$  ensembles, and NEMD simulations with applied thermal gradient, were repeated in sequence to get the final tensile strain-dependent  $\lambda$  results.

### 3. Results and discussion

#### 3.1 Effect of polymorphs on thermal conductivity of CNCs

We first calculated the thermal conductivities for different polymorphs  $I\alpha$ ,  $I\beta$ , II, III<sub>1</sub>. The same effective chain length for these polymorphs was used together with the smallest number of chains to form a crystalline unit cell (Fig. 1b). As summarized in Table 2, these four polymorphs show thermal conductivities  $\lambda$  in the range of 3.5~6.2 W/(m·K). The differences in thermal conductivity may arise from the different stacking of chains to form the crystalline lattices, especially from the different cross-sectional areas defined by the polymorph parameters (Table 1). By computing the thermal conductance  $TC$ , which is only dependent on the transferred thermal energy  $Q$  and temperature difference  $\Delta T$  in the form of  $TC = Q / \Delta T$  (excluding the polymorph parameters of CNCs), we found that a single chain in all these four polymorphs

yields similar  $TC$  values (around 100 pW/K) (Table 2). This result suggests that heat transfer capacity of each chain is weakly affected by the polymorphs of CNCs. It gives a convenient way to estimate the overall thermal conductance of CNCs with various polymorphs.

Table 2. Thermal conductivities  $\lambda$  of CNCs with polymorphs  $I\alpha$ ,  $I\beta$ , II,  $III_1$  at 300 K.  $TC$  is the thermal conductance per single chain in these polymorphs.

	$I\alpha$	$I\beta$	II	$III_1$
$L$ (nm)	11.4	11.4	11.4	11.4
$A$ (nm <sup>2</sup> )	0.79	1.58	1.63	0.67
$\lambda$ (W/(m·K))	5.8	3.6	3.5	6.2
$TC$ (pW/K)	99.8	101.3	100.7	91.1

We also calculated the phonon density of states (PDOS) of these four CNC polymorphs, which are derived from discrete Fourier transform of the velocity autocorrelation function:

$$D(\omega) = \int_0^{\tau} \langle v(0) \cdot v(t) \rangle \exp(-i\omega t) dt \quad (2)$$

where  $D(\omega)$  is the PDOS at a frequency of  $\omega$  and  $\langle v(0) \cdot v(t) \rangle$  is the correlation function of atomic velocities. The velocities were correlated every 0.1 fs in a total integration time of 0.02 ns in a typical equilibrium MD simulation with an  $NVT$  ensemble. Fig. 3 shows the PDOS of C and O atoms for all the polymorphs with parameters listed in Table 2. These PDOS are not quite distinguishable from one another, again indicating similar phonon properties for these different crystalline structures. There is one main peak for O atom centered around 5 THz, while the main

peaks for C atoms are significantly smaller than that of O atoms and distribute in a broader range of 0~20 THz. This suggests that the O atoms carry the majority of low frequency phonons. The disparity between the phonon populations of O and C atoms could induce strong phonon anharmonic scattering and thus decrease the overall thermal conductivity [40].

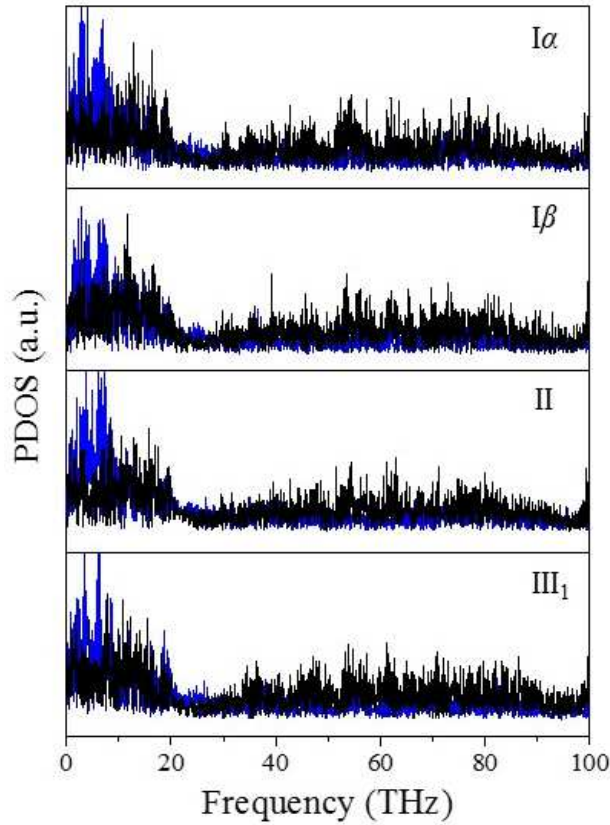


Figure 3. Comparison of phonon density of states (PDOS) of polymorphs  $I\alpha$ ,  $I\beta$ , II,  $III_1$  with parameters listed in Table 2 at 300 K. Black and blue curves denote C and O atoms, respectively.

### 3.2 Effects of system size and temperature on thermal conductivity of CNCs

Using  $I\beta$  as a model polymorph, we further studied how the thermal conductivity depends on the system size. It is well known that the size-dependent thermal conductivity is an indicator

of ballistic-diffusive transport, typically occurring in nanosystems [41]. In Fig. 4a, the thermal conductivities  $\lambda$  were plotted against different system effective length  $L$ , showing the monotonic increase of  $\lambda$  with  $L$ . The increase of chain length promotes more ballistic transports of the phonons with an increased phonon mean free path (MFP) along the chain direction, leading to enhanced thermal conductivity. We should emphasize that the size effect observed here is prominent and it is exactly the major difference between the nanoscale systems and bulk systems. The size effect is also used as a tool to measure the ballistic-diffusive transport of phonons, and to guide how to control the thermal conductivity of nanosystems, as reported in recent experiments and corresponding MD simulations [42–45]. The values we obtained in Fig. 4, as defined above, should be interpreted as effective thermal conductivities, and the value should be referred to only when the nanoscale size parameters are explicitly specified.

It is also possible to extrapolate the MD results to the bulk value, but special care should be taken. Here, through Boltzmann transport equation and the Matthiessen's rule, the inverse of the thermal conductivity  $\lambda(L)^{-1}$  and the inverse of the sample length  $L^{-1}$  should have linear relationship in the form of [38,46]

$$\lambda(L)^{-1} = \lambda_{\infty}^{-1} (1 + l/L) \quad (3)$$

where  $\lambda_{\infty}^{-1}$  is the inverse of bulk thermal conductivity and  $l$  is the effective phonon MFP. We attempted to extrapolate the data of a single cellulose chain of Fig. 4a to an infinitely long chain and obtained  $\lambda_{\infty} = 6.4 \text{ W}/(\text{m} \cdot \text{K})$  and phonon MFP  $l = 6.8 \text{ nm}$  (inset of Fig. 4a). The value of  $\lambda_{\infty}$  is about 100 folds higher than that of traditional bulk cellulose polymers reported experimentally. It implies the potential of enhancing thermal transport by using nanotechnology, and experimental realizations are required to check its feasibility.

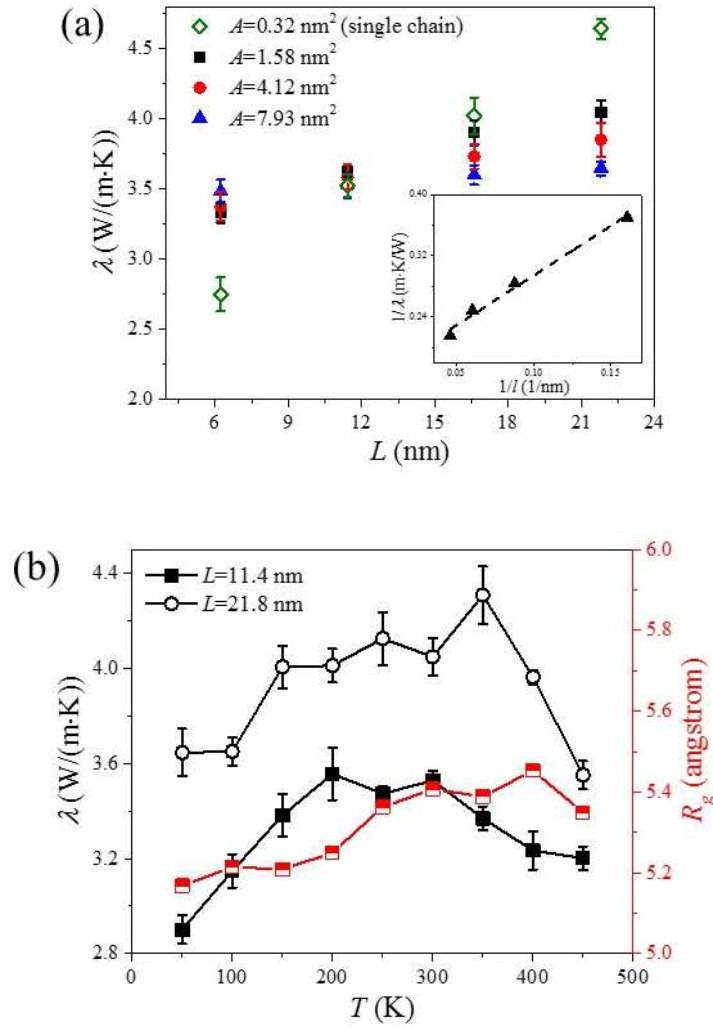


Figure 4. (a) Size dependence of thermal conductivities of  $I\beta$  CNCs at 300K with different length  $L$  and cross-sectional area  $A$ . The inset shows the fitting process to Eq. (3) by plotting the inverse thermal conductivity of single chain CNC against the inverse chain length. (b) Dependence of thermal conductivity of single chain CNC against the inverse chain length. (c) Dependence of thermal conductivities of  $I\beta$  CNCs on temperature at effective length  $L=11.4$  nm and 21.8 nm. Both cases have the cross-sectional area  $A=1.58$  nm<sup>2</sup>. The radius of gyration  $R_g$  for  $L=11.4$  nm CNCs is also shown.

A more interesting behavior arises when we changed the cross-sectional area  $A$  in Fig. 4a. We started from one single chain with  $A=0.32 \text{ nm}^2$  to  $I\beta$  crystalline lattice of 25 chains with a total  $A=7.93 \text{ nm}^2$ . While  $\lambda$  generally decreases with an increase in  $A$  due to more interchain phonon scattering [28], the opposite trend was observed at small effective length and the crossover in the plot. Plausibly, at small chain length, the ballistic transport may contribute more significantly to thermal conductivity, which is effectively blocked by the small cross-sectional area due to the scattering at the boundaries. Therefore, there are two competing effects resulting from interchain scattering and boundary scattering, which may lead to different dependence of  $\lambda$  on the cross-sectional area  $A$  with different system lengths. Using Eq. 3, we obtained the phonon MFPs of 2.08, 1.33, and 0.48 nm for  $A=1.58, 4.12, \text{ and } 7.93 \text{ nm}^2$ , respectively, suggesting that the interchain scattering would strongly undermine the ballistic phonon transport and lead to a drastically decreased MFP. In this respect, the high thermal conductivity of CNCs is enabled by the low-dimensional effect, which is similar to what observed with graphene and carbon nanotubes [47]. The size-dependence crossover behavior indicates the rich tunability of  $\lambda$  by utilizing ballistic-diffusive phonon transport in nanoscale. Some existing experimental studies [14] also reported the thermal conductivity of nanocellulose sheets, but with crystallite sizes (length:  $\sim 300 \text{ nm}$ , cross-sectional area:  $6.0\sim 64.0 \text{ nm}^2$ ) much larger than our simulations. The measured in-plane  $\lambda$  varies from 0.6 to 2.5  $\text{W}/(\text{m}\cdot\text{K})$ , which is in the same magnitude but smaller than our results of 3.6  $\text{W}/(\text{m}\cdot\text{K})$  at  $L=21.8 \text{ nm}$ ,  $A=7.93 \text{ nm}^2$ . Besides the big mismatch of system sizes between simulations and experiments, the samples in experiments suffer from random fiber orientation, low crystallinity and interfacial thermal resistance [14]. All these effects might hinder the effective ballistic phonon transport and lead to a smaller thermal conductivity compared to our simulation results of a single crystal. Although this is not a direct comparison

between data points at the exact conditions, it implies the reasonability of our calculated results. Future efforts are needed to directly compare experiments and simulations with advanced measurement approach, sample preparation and multiple-scale simulation.

In addition to system size, we also studied the effects of system temperatures on thermal conductivities of  $I\beta$  CNCs. The results are depicted in Fig. 4b. For the two tested lengths  $L$ , the thermal conductivity first increases with temperature  $T$ , and then decreases. The maximum peak of  $\lambda$  appears at around 200 K for  $L=11.4$  nm, and at around 350 K for  $L=21.8$  nm. To understand this temperature dependence, we first calculated the radius of gyration  $R_g$  of CNCs [28]:

$$R_g = \sqrt{\frac{1}{M} \sum_i m_i \left[ (x_i - x_{cm})^2 + (y_i - y_{cm})^2 \right]} \quad (4)$$

Here,  $M$  is the total mass of CNCs,  $m_i$  is the mass of atom  $i$  in the backbone, and  $x_{cm}$ ,  $y_{cm}$  are the coordinates of the center of mass. It was found that  $R_g$  shows similar dependence on temperature, but the curve slightly shifts to higher temperature region compared to that of  $\lambda$ . This result is in agreement with that reported for amorphous PE systems [48]. Moreover, it has been demonstrated that for crystalline materials,  $\lambda$  decreases with increasing temperature due to the stronger phonon Umklapp scattering [49]. The opposite trend at low  $T$  may arise from the anharmonicity of the disordered structure of the cellulose chains, with an underlying thermal transport mechanism of energy hopping among localized modes, which leads to an increased  $\lambda$  with the increasing temperature [50]. It could be thus inferred that CNCs possess the feature of both crystalline and disordered structures. Although the observed temperature variation of  $\lambda$  for CNC, within 1.0 W/(m·K), is much smaller than that of metals and semiconductors, it may however have some benefits in cases that prefer a near-constant thermal conductivity under the condition of large temperature fluctuations.

### 3.3 Effect of mechanical strains on thermal conductivity of CNCs

We also attempted to tune the thermal conductivities of CNCs by applying mechanical strains along the chain direction. Fig. 5 shows the variation of  $\lambda$  on strains for  $I\beta$  CNCs with different lengths and cross-sections and three other polymorphs  $I\alpha$ , II, III<sub>1</sub> with the sizes depicted in Table 2. As expected, we observed the monotonic increases for all the cases up to the strain of 0.11. Further stretching may cause the bond breakage in the cellulose chains. The CNCs ( $I\beta$  CNC)

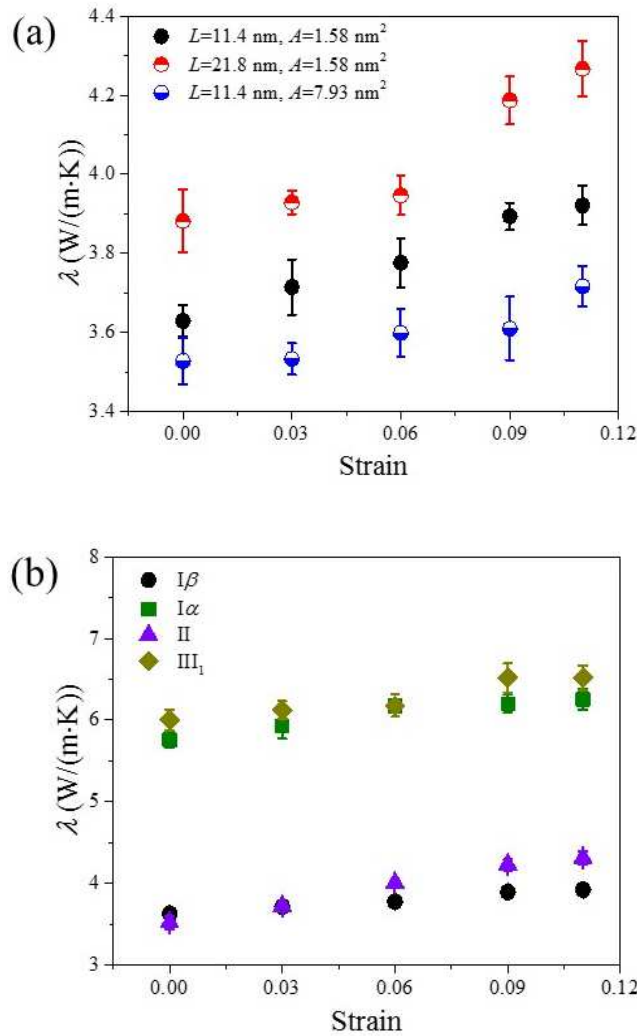


Figure 5. Dependence of thermal conductivities on mechanical strains at 300K. (a) I $\beta$  CNCs with different effective lengths and cross-sectional areas. (b) Different crystalline structures with their sizes the same with Table 2.

with smaller cross-sectional area (1.58 nm<sup>2</sup>) obtained about 8% increase of  $\lambda$  when the strain is increased from 0 to 0.11, while the ones with larger cross-sectional area (7.93 nm<sup>2</sup>) only have about 4% increase. Such enhancement of thermal conductivity due to stretching can be correlated with the morphological change of the polymer chains. We calculated the orientational order parameter, also known as the Herman's orientation function, which is a useful indicator for chain alignment [31]:

$$P_2 = 1.5 \langle \mathbf{e}_i \cdot \mathbf{e}_z \rangle - 0.5 \quad (5)$$

Here,  $\mathbf{e}_z$  is the unit vector parallel to the applied strain; and  $\mathbf{e}_i$  is the local chain direction at the selected atom  $i$ , which is computed as  $\mathbf{e}_i = (\mathbf{r}_{i+1} - \mathbf{r}_{i-1}) / |\mathbf{r}_{i+1} - \mathbf{r}_{i-1}|$ , where  $r_{i+1}$  and  $r_{i-1}$  are the distances to atom  $i$  from the two nearest neighbors. We chose the O atom, which connects the two glucose rings as atom  $i$  and the nearest two C atoms as atoms  $i+1$  and  $i-1$  (Fig. 1a). The stretching of CNCs may also induce the suppression of the wavy motion of chains, which can be quantified by the radius of gyration  $R_g$ . The results for  $P_2$  and  $R_g$  are shown in Fig. 6, and as expected, there exists a positive correlation between the strain-tuned thermal conductivity  $\lambda$  and  $P_2$  and a negative correlation between  $\lambda$  and  $R_g$ . The enhanced chain alignment can increase the phonon MFP compared to the more randomly oriented counterparts and thus lead to an enhanced thermal conductivity.

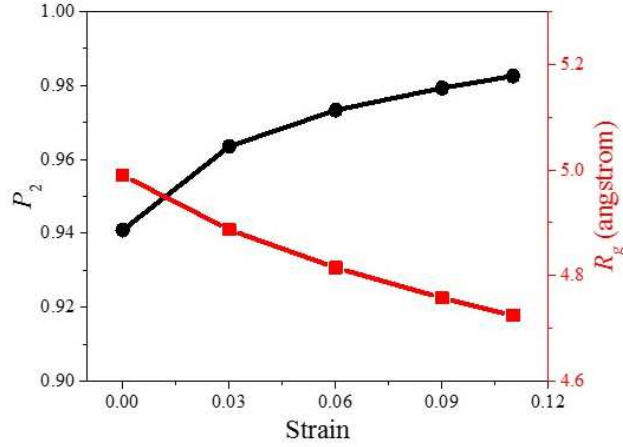


Figure 6. Variation of radius of gyration ( $R_g$ ) and orientational order of  $I\beta$  CNC with  $L=11.4$  nm,  $A=1.58$  nm<sup>2</sup> on tensile strain.

The effect of tensile strain on the PDOS is shown in Fig. 7, from which we can observe a very slight shift towards the lower frequency regime in the 0~10 THz of O atoms and 0~20 THz of C atoms. However, the shift to the lower regime in the relatively high frequency range of 20~80 THz is more pronounced when CNCs are stretched. As the low frequency phonon vibrations contribute more significantly than high frequency ones to thermal transport, a slight influence on the thermal conductivity should be expected from the PDOS analyses here, which actually agrees with our simulation results in Fig. 5. This small effect can be attributed to the fact that these cellulose chains are already well aligned in the unstrained samples (Fig. 6,  $P_2=0.94$ ), and the strain up to 0.11 only slightly improves the alignment (Fig. 6,  $P_2=0.98$ ).

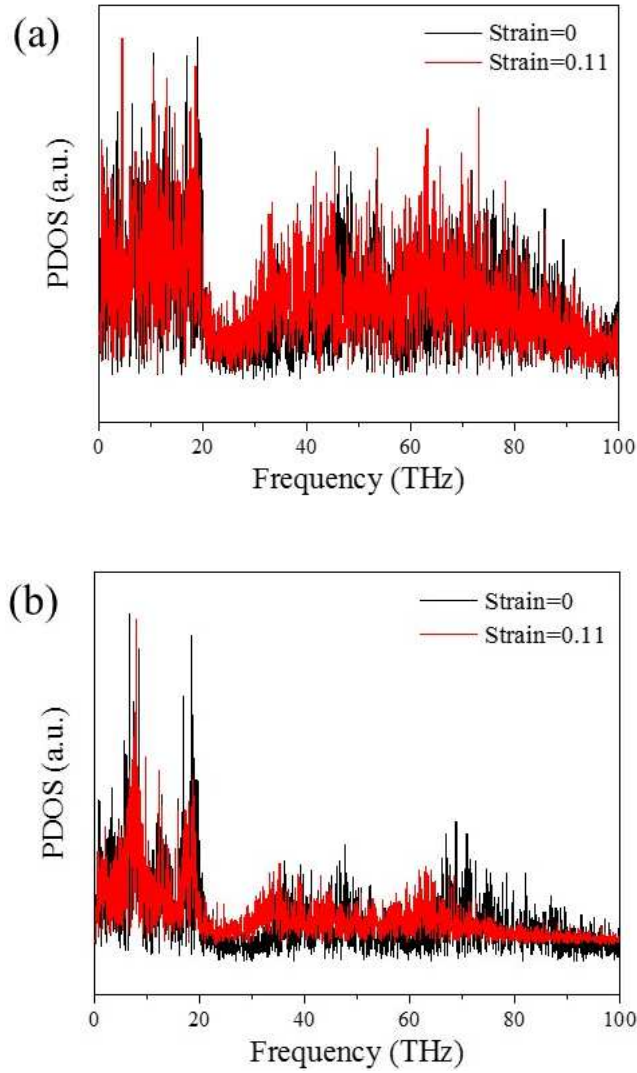


Figure 7. Phonon density of states (PDOS) at different tensile strains for  $I\beta$  CNCs with  $L=11.4$  nm,  $A=1.58$  nm<sup>2</sup> at 300 K. (a) PDOS of C atoms; (b) PDOS of O atoms.

#### 4. Conclusions

In this work, the thermal conductivities of CNCs were calculated by nonequilibrium MD simulations. We found that the thermal conductivity depends on the crystalline structures of CNC polymorphs (i.e.,  $I\alpha$ ,  $I\beta$ , II, III<sub>1</sub>), but the thermal conductance of unit chain for each

polymorph is similar. The extrapolation to an infinitely long single chain yields a thermal conductivity of  $\sim 6$  W/(m·K), implying CNCs' potential as high thermal conductive polymer. We also studied the effect of the system size by changing the chain length and cross-section of  $I\beta$  CNCs, and found the monotonic increase of thermal conductivities with chain length due to the enhancement of ballistic phonon transport. However, the crossover upon the change in the cross-sectional area at different chain lengths suggests two competing effects from phonon boundary scattering and interchain scattering. Temperature effects indicate that the CNCs possess the dual feature of both crystalline and disordered structures, which is reflected by an increase of thermal conductivity followed by a decrease with increasing temperature. Further investigation of mechanical strains along the chain direction reveals the increase of the thermal conductivities, which can be correlated with the increased chain alignment and the slight shift to the lower frequency regime of the PDOS of C and O atoms.

## Acknowledgements

The authors acknowledge financial support from US Department of Energy (Award number: DE-FE0031645), National Science Foundation (Award number: 1933861, 1825352). The calculations were performed on the HPC resources at the University of Missouri Bioinformatics Consortium (UMBC), supported in part by NSF (award number: 1429294).

## References

- [1] R.J. Moon, A. Martini, J. Nairn, J. Simonsen, J. Youngblood, Cellulose nanomaterials review: structure, properties and nanocomposites, *Chem. Soc. Rev.* 40 (2011) 3941.

- [2] A. Dufresne, Nanocellulose: a new ageless bionanomaterial, *Mater. Today*. 16 (2013) 220–227.
- [3] S. Kalia, A. Dufresne, B.M. Cherian, B.S. Kaith, L. Avérous, J. Njuguna, E. Nassiopoulos, Cellulose-based bio- and nanocomposites: A review, *Int. J. Polym. Sci.* 2011 (2011) 1–35.
- [4] N. Mittal, F. Ansari, V. Gowda Krishne, C. Brouzet, P. Chen, P.T. Larsson, S. V. Roth, F. Lundell, L. Wågberg, N.A. Kotov, L.D. Söderberg, Multiscale Control of Nanocellulose Assembly: Transferring Remarkable Nanoscale Fibril Mechanics to Macroscale Fibers, *ACS Nano*. 12 (2018) 6378–6388.
- [5] J. Song, C. Chen, S. Zhu, M. Zhu, J. Dai, U. Ray, Y. Li, Y. Kuang, Y. Li, N. Quispe, Y. Yao, A. Gong, U.H. Leiste, H.A. Bruck, J.Y. Zhu, A. Vellore, H. Li, M.L. Minus, Z. Jia, A. Martini, T. Li, L. Hu, Processing bulk natural wood into a high-performance structural material, *Nature*. 554 (2018) 224–228.
- [6] T. Li, Y. Zhai, S. He, W. Gan, Z. Wei, M. Heidarinejad, D. Dalgo, R. Mi, X. Zhao, J. Song, J. Dai, C. Chen, A. Aili, A. Vellore, A. Martini, R. Yang, J. Srebric, X. Yin, L. Hu, A radiative cooling structural material, *Science*. 364 (2019) 760–763.
- [7] J. Huang, H. Zhu, Y. Chen, C. Preston, K. Rohrbach, J. Cumings, L. Hu, Highly transparent and flexible nanopaper transistors, *ACS Nano*. 7 (2013) 2106–2113.
- [8] J. Sheng, S. Tong, Z. He, R. Yang, Recent developments of cellulose materials for lithium-ion battery separators, *Cellulose*. 24 (2017) 4103–4122.
- [9] Y.-D. He, Z.-L. Zhang, J. Xue, X.-H. Wang, F. Song, X.-L. Wang, L.-L. Zhu, Y.-Z. Wang, Biomimetic optical cellulose nanocrystal films with controllable iridescent color and environmental stimuli-responsive chromism, *ACS Appl. Mater. Interfaces*. 10 (2018) 5805–5811.
- [10] S.T. Nguyen, J. Feng, S.K. Ng, J.P.W. Wong, V.B.C. Tan, H.M. Duong, Advanced thermal insulation and absorption properties of recycled cellulose aerogels, *Colloids Surfaces A Physicochem. Eng. Asp.* 445 (2014) 128–134.
- [11] H. Sehaqui, M. Salajková, Q. Zhou, L.A. Berglund, Mechanical performance tailoring of tough ultra-high porosity foams prepared from cellulose i nanofiber suspensions, *Soft Matter*. 6 (2010) 1824–1832.
- [12] Y. Kobayashi, T. Saito, A. Isogai, Aerogels with 3D ordered nanofiber skeletons of liquid-crystalline nanocellulose derivatives as tough and transparent insulators, *Angew. Chem. Int. Ed. Engl.* 53 (2014) 10394–10397.
- [13] M. Obori, D. Suh, S. Yamasaki, T. Kodama, T. Saito, A. Isogai, J. Shiomi, Parametric model to analyze the components of the thermal conductivity of a cellulose-nanofibril aerogel, *Phys. Rev. Appl.* 11 (2019) 024044.
- [14] K. Uetani, T. Okada, H.T. Oyama, Crystallite size effect on thermal conductive properties of nonwoven nanocellulose sheets, *Biomacromolecules*. 16 (2015) 2220–2227.
- [15] A. Henry, G. Chen, High thermal conductivity of single polyethylene chains using molecular dynamics simulations, *Phys. Rev. Lett.* 101 (2008) 235502.

- [16] B.-Y. Cao, Y.-W. Li, J. Kong, H. Chen, Y. Xu, K.-L. Yung, A. Cai, High thermal conductivity of polyethylene nanowire arrays fabricated by an improved nanoporous template wetting technique, *Polymer (Guildf)*. 52 (2011) 1711–1715.
- [17] K. Kurabayashi, Anisotropic thermal properties of solid polymers, *Int. J. Thermophys.* 22 (2001) 277–288.
- [18] S. Shen, A. Henry, J. Tong, R. Zheng, G. Chen, Polyethylene nanofibres with very high thermal conductivities, *Nat. Nanotechnol.* 5 (2010) 251–255.
- [19] Y. Xu, D. Kraemer, B. Song, Z. Jiang, J. Zhou, J. Loomis, J. Wang, M. Li, H. Ghasemi, X. Huang, X. Li, G. Chen, Nanostructured polymer films with metal-like thermal conductivity, *Nat. Commun.* 10 (2019) 1771.
- [20] V. Singh, T.L. Bougher, A. Weathers, Y. Cai, K. Bi, M.T. Pettes, S.A. McMenamin, W. Lv, D.P. Resler, T.R. Gattuso, D.H. Altman, K.H. Sandhage, L. Shi, A. Henry, B.A. Cola, High thermal conductivity of chain-oriented amorphous polythiophene, *Nat. Nanotechnol.* 9 (2014) 384–390.
- [21] G.H. Kim, D. Lee, A. Shanker, L. Shao, M.S. Kwon, D. Gidley, J. Kim, K.P. Pipe, High thermal conductivity in amorphous polymer blends by engineered interchain interactions, *Nat. Mater.* 14 (2015) 295–300.
- [22] K. Uetani, T. Okada, H.T. Oyama, In-plane anisotropic thermally conductive nanopapers by drawing bacterial cellulose hydrogels, *ACS Macro Lett.* 6 (2017) 345–349.
- [23] J.A. Diaz, Z. Ye, X. Wu, A.L. Moore, R.J. Moon, A. Martini, D.J. Boday, J.P. Youngblood, Thermal conductivity in nanostructured films: from single cellulose nanocrystals to bulk films, *Biomacromolecules.* 15 (2014) 4096–4101.
- [24] J. Sun, Y. Yao, X. Zeng, G. Pan, J. Hu, Y. Huang, R. Sun, J. Bin Xu, C.P. Wong, Preparation of Boron Nitride Nanosheet/Nanofibrillated Cellulose Nanocomposites with Ultrahigh Thermal Conductivity via Engineering Interfacial Thermal Resistance, *Adv. Mater. Interfaces.* 4 (2017) 1–10.
- [25] H. Bao, J. Chen, X. Gu, B. Cao, A review of simulation methods in micro/nanoscale heat conduction, *ES Energy Environ.* 1 (2018) 16–55.
- [26] R. Muthaiah, J. Garg, Temperature effects in the thermal conductivity of aligned amorphous polyethylene—A molecular dynamics study, *J. Appl. Phys.* 124 (2018) 105102.
- [27] V. Rashidi, E.J. Coyle, K. Sebeck, J. Kieffer, K.P. Pipe, Thermal conductance in cross-linked polymers: effects of non-bonding interactions, *J. Phys. Chem. B.* 121 (2017) 4600–4609.
- [28] T. Luo, K. Esfarjani, J. Shiomi, A. Henry, G. Chen, Molecular dynamics simulation of thermal energy transport in polydimethylsiloxane, *J. Appl. Phys.* 109 (2011) 074321.
- [29] T. Lu, K. Kim, X. Li, J. Zhou, G. Chen, J. Liu, Thermal transport in semicrystalline polyethylene by molecular dynamics simulation, *J. Appl. Phys.* 123 (2018) 015107.
- [30] H. Ma, Z. Tian, Effects of polymer topology and morphology on thermal transport: A

- molecular dynamics study of bottlebrush polymers, *Appl. Phys. Lett.* 110 (2017) 091903.
- [31] T. Zhang, T. Luo, High-contrast, reversible thermal conductivity regulation utilizing the phase transition of polyethylene nanofibers, *ACS Nano.* 7 (2013) 7592–7600.
- [32] A.C. O’Sullivan, Cellulose: The structure slowly unravels, *Cellulose.* 4 (1997) 173–207.
- [33] T.C.F. Gomes, M.S. Skaf, Cellulose-builder: A toolkit for building crystalline structures of cellulose, *J. Comput. Chem.* 33 (2012) 1338–1346.
- [34] S. Plimpton, Fast parallel algorithms for short-range molecular dynamics, *J. Comput. Phys.* 117 (1995) 1–19.
- [35] A.C.T. Van Duin, S. Dasgupta, F. Lorant, W.A. Goddard, ReaxFF: A reactive force field for hydrocarbons, *J. Phys. Chem. A.* 105 (2001) 9396–9409.
- [36] K. Chenoweth, A.C.T. Van Duin, W.A. Goddard, ReaxFF reactive force field for molecular dynamics simulations of hydrocarbon oxidation, *J. Phys. Chem. A.* 112 (2008) 1040–1053.
- [37] M. Buerkle, Y. Asai, Thermal conductance of Teflon and Polyethylene: Insight from an atomistic, single-molecule level, *Sci. Rep.* 7 (2017) 41898.
- [38] Y. Dong, M. Meng, M.M. Groves, C. Zhang, J. Lin, Thermal conductivities of two-dimensional graphitic carbon nitrides by molecule dynamics simulation, *Int. J. Heat Mass Transf.* 123 (2018) 738–746.
- [39] A. Henry, Thermal transport in polymers, *Annu. Rev. Heat Transf.* 17 (2014) 485–520.
- [40] Y. Dong, C. Diao, Y. Song, H. Chi, D.J. Singh, J. Lin, Molecular bridge thermal diode enabled by vibrational mismatch, *Phys. Rev. Appl.* 11 (2019) 024043.
- [41] G. Chen, Ballistic-diffusive heat-conduction equations, *Phys. Rev. Lett.* 86 (2001) 2297–2300.
- [42] X. Xu, L.F.C. Pereira, Y. Wang, J. Wu, K. Zhang, X. Zhao, S. Bae, C. Tinh Bui, R. Xie, J.T.L. Thong, B.H. Hong, K.P. Loh, D. Donadio, B. Li, B. Özyilmaz, Length-dependent thermal conductivity in suspended single-layer graphene, *Nat. Commun.* 5 (2014) 1–6.
- [43] H. Wang, S. Hu, K. Takahashi, X. Zhang, H. Takamatsu, J. Chen, Experimental study of thermal rectification in suspended monolayer graphene, *Nat. Commun.* 8 (2017) 15843.
- [44] W. Ma, Y. Liu, S. Yan, T. Miao, S. Shi, M. Yang, X. Zhang, C. Gao, Systematic characterization of transport and thermoelectric properties of a macroscopic graphene fiber, *Nano Res.* 9 (2016) 3536–3546.
- [45] W. Ma, Y. Liu, S. Yan, T. Miao, S. Shi, Z. Xu, X. Zhang, C. Gao, Chemically doped macroscopic graphene fibers with significantly enhanced thermoelectric properties, *Nano Res.* 11 (2018) 741–750.
- [46] S. Lin, M.J. Buehler, Thermal transport in monolayer graphene oxide: atomistic insights into phonon engineering through surface chemistry, *Carbon N. Y.* 77 (2014) 351–359.

- [47] C. Diao, Y. Dong, J. Lin, Reactive force field simulation on thermal conductivities of carbon nanotubes and graphene, *Int. J. Heat Mass Transf.* 112 (2017) 903–912.
- [48] T. Zhang, T. Luo, Role of chain morphology and stiffness in thermal conductivity of amorphous polymers, *J. Phys. Chem. B.* 120 (2016) 803–812.
- [49] V. Goyal, A.A. Balandin, Thermal properties of the hybrid graphene-metal nano-micro-composites: Applications in thermal interface materials, *Appl. Phys. Lett.* 100 (2012) 073113.
- [50] P.B. Allen, J.L. Feldman, Thermal conductivity of glasses: Theory and application to amorphous Si, *Phys. Rev. Lett.* 62 (1989) 645–648.